RESEARCH ARTICLE | NOVEMBER 08 2024

Interference effects in commercially available free-space silicon single-photon avalanche diodes

Special Collection: Advances in Quantum Metrology

L. Arabskyj 🜌 📵 ; B. Dejen 📵 ; T. S. Santana 💿 ; M. Lucamarini 📵 ; C. J. Chunnilall 📵 ; P. R. Dolan 📵



Appl. Phys. Lett. 125, 194003 (2024) https://doi.org/10.1063/5.0225337





Articles You May Be Interested In

A refined method for characterizing afterpulse probability in single-photon avalanche diodes

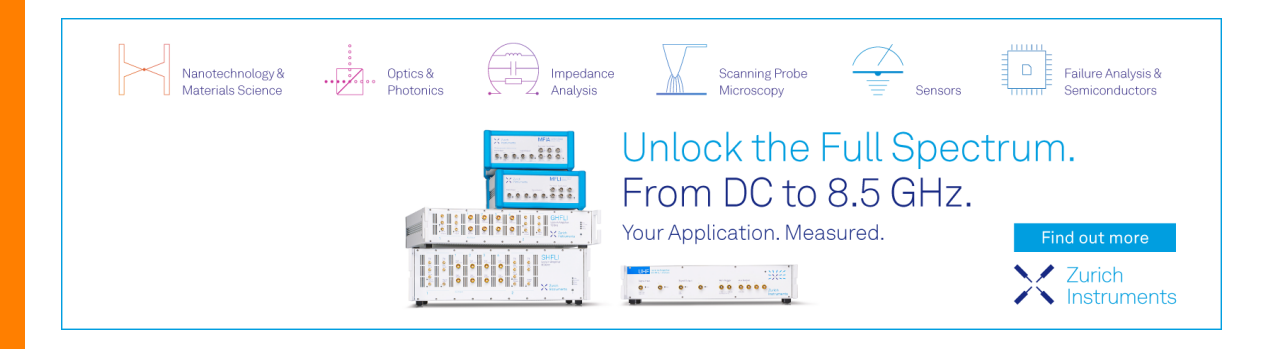
Appl. Phys. Lett. (November 2024

Detection of ultra-weak laser pulses by free-running single-photon detectors: Modeling dead time and dark counts effects

Appl. Phys. Lett. (April 2021)

Low-noise low-jitter 32-pixels CMOS single-photon avalanche diodes array for single-photon counting from 300 nm to 900 nm

Rev. Sci. Instrum. (December 2013)





Interference effects in commercially available free-space silicon single-photon avalanche diodes

Cite as: Appl. Phys. Lett. 125, 194003 (2024); doi: 10.1063/5.0225337 Submitted: 24 June 2024 · Accepted: 25 October 2024 · Published Online: 8 November 2024

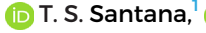


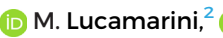


















AFFILIATIONS

¹National Physical Laboratory, Hampton Road, Teddington TW11 OLW, United Kingdom

 2 School of Physics, Engineering & Technology and York Centre for Quantum Technologies, Institute for Safe Autonomy, University of York, York YO10 5FT, United Kingdom

Note: This paper is part of the APL Special Collection on Advances in Quantum Metrology.

a) Author to whom correspondence should be addressed: luke.arabskyj@npl.co.uk

ABSTRACT

Single-photon avalanche diodes (SPADs) are essential for photon-based measurements and metrology, enabling measurement comparisons at the few-photon level and facilitating global traceability to the SI. A spatially uniform detector response is crucial for these applications. Here, we report on interference effects in commercially available silicon SPADs that are detrimental to their spatial uniformity. Contrasts as high as 18% are observed, posing problems for metrology and general applications that utilize coherent light and require stable detection efficiencies. We eliminate the device optical window as a contributing interface, isolating likely causes to anti-reflective coatings, the semiconductor surface, and the SPAD's internal structure. We also present results where we leverage this sub-optimal behavior by aligning an incident beam with the position of maximum constructive interference, yielding an effective detection efficiency of 51.1(1.7)% compared to the normal value of 44.3(1)% obtained with the interference suppressed. We anticipate that this work will significantly impact the continuing development of these devices, the methods for characterizing them, and their use in accurate measurements.

© 2024 Author(s). All article content, except where otherwise noted, is licensed under a Creative Commons Attribution-NonCommercial 4.0 International (CC BY-NC) license (https://creativecommons.org/licenses/by-nc/4.0/). https://doi.org/10.1063/5.0225337

Silicon single-photon avalanche diode (SPAD) detectors are costeffective, compact, portable, and operate at near-room temperature and offer timing resolution of the order of hundreds of picoseconds. With a typical peak efficiency of 70% at a wavelength around 600 nm, these characteristics make them a compelling option for many applications that utilize the particle nature of light, including light detection and ranging (LiDAR) for autonomous vehicles, 2,3 security and surveillance,4 biomedical imaging,5,6 and quantum information.1,7 They are also especially critical to metrology, 8-11 enabling the comparison of optical radiation scales at the few-photon level. 12-16 Such measurement comparisons are fundamental to metrology, ensuring consistency and enhancing global measurement equivalence.

The primary performance metric is often the single-photon detection efficiency (DE), which is defined as the probability of an incident photon producing a measurable output signal, while the detector is on and ready to detect. 1,17 It is especially critical to applications that require high detection rates, such as quantum key distribution For free-space applications, the position of the incident excitation beam may vary significantly with time.^{23–26} Although compensation methods can be employed,²⁷ detectors with a uniform spatial response are desirable, particularly in measurement comparisons, where a non-uniform response can be the limiting factor.²⁸ Response uniformity is measured by mapping the detector's response as a function of incident beam position. Recently, interference fringes with a contrast up to $\approx 10\%$ were reported in the spatial response of a commercially available SPAD when mapped with a 20 μ m beam.²⁹ The source of interference was speculated to originate from reflections between the TO-can window surfaces and the detector. Although the interference was suppressed by switching to a pulsed source with a relatively short coherence time (pulse durations of 150 fs), this approach may not be possible for all users. Furthermore, in many applications, phase coherence is a critical parameter^{30–33} and, therefore, must be maintained. Similar interference fringes have been observed at the National Physical Laboratory (NPL) and at the Istituto Nazionale di Ricerca Metrologica³⁴ (INRiM); however, we note that they are not consistently observed in other works, 12,35 highlighting a gap in current understanding.

In this work, we characterize the spatial response of SPADs in unprecedented detail, uncovering interference fringes that are detrimental to uniformity. By examining commercial devices from different manufacturers, we observe fringe contrasts that are significantly greater in amplitude than those previously reported.²⁹ We also eliminate the TO-can window as a source of the interference. Finally, we present a result where we leverage this non-ideal behavior, increasing a detector's efficiency to a value well above the manufacturer's specified DE.

The experimental method selected for spatial-response mapping was a 4f optical setup, chosen for its ability to quickly scan the focal plane with high resolution. The setup is illustrated in Fig. 1 where the laser source is coupled into free-space from a single-mode (SM) fiber (top right) before being collimated by a Mitutoyo apochromatic objective lens (MY10X-823, 0.26 NA) labeled L_1 . The collimated beam was then incident upon a Newport sub-microradian Fast Beam Steering Mirror (FSM-300-01) before being focused and recollimated by $f=125 \,\mathrm{mm}$ achromatic doublets, L_2 and L_3 , forming a one-to-one relay. A second Mitutoyo objective lens was then used to focus the beam into an $\approx 5 \,\mu \text{m}$ diameter Gaussian spot with which the plane of the sensor surface was aligned. To protect the sensor from ambient light, a neutral density (ND) filter with a broadband anti-reflective coating (ARC) spanning 650-1050 nm was attached to the SPAD housing using a custom-made light-tight fixture. It is important to note that the interference described here is independent of all these components, with the exception of the SPAD, which is shown later.

The spatial response of each detector was measured using two sources: (1) a CW 852 nm pigtailed laser diode (Thorlabs LP852-SF60); (2) a Ti:Sapphire mode-locked laser producing 14 ps duration pulses at a repetition rate of 80 MHz, centered at a wavelength of 890 nm. Source 1 was operated below its lasing threshold, which effectively suppresses interference. This is referred to as the incoherent source. In contrast to source 1, the coherent source 2 has the ability to cause interference, making it the chosen source for characterizing the interference fringes. The wavelength difference of source 2 was due to its commitment to other long-term experiments at 890 nm. While the laser diode operated above threshold may be used as a coherent source, the Ti:Sapphire laser was selected to replicate the conditions of applications that utilize discrete pulses, such as QKD.

Detectors commercially available from two manufacturers were evaluated. All utilize sensors based upon back-illuminated reach-

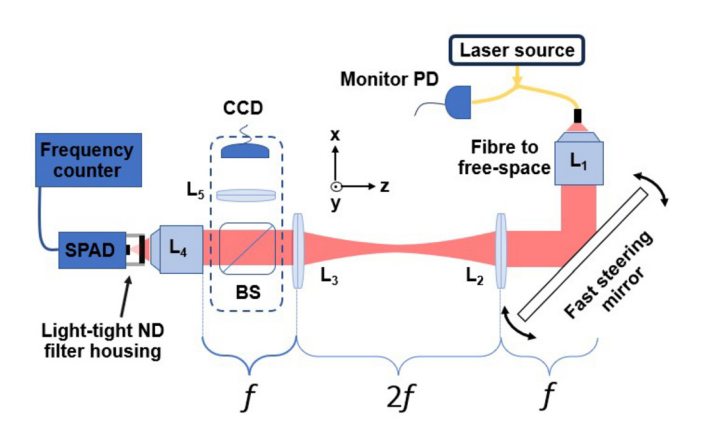


FIG. 1. Schematic of the 4f setup used to characterize each detector's spatial response. The dashed rectangle between lenses L₃ and L₄ marks the wide-field imaging system, which is discussed in the later text. Acronyms: ND-neutral density, BS-beam splitter (pellicle), PD-photodiode, CCD-charge coupled device, SPAD—single-photon avalanche diode.

through designs that were developed to maximize DE in the nearinfrared region of the spectrum. 36,37 The detectors from manufacturer A (2 detectors, same model) had a sensor diameter of 180 μ m, whereas those from manufacturer B (2 detectors, same model) had a sensor diameter of 500 μ m. Scans were performed in small steps ($\approx 1 \mu$ m) in the (x, y) plane, sampling for 20 ms at each point. The laser light was attenuated such that each detector's count rate was approximately 10⁵ cps, providing a signal-to-background ratio greater than 100.

The normalized spatial response maps of the four detectors are displayed in Fig. 2. The four uppermost maps [Figs. 2(a)-2(d)] correspond to the two detectors from manufacturer A. Detectors are separated in rows, and columns divide incoherent and coherent illumination. The four lowermost maps belong to detectors from

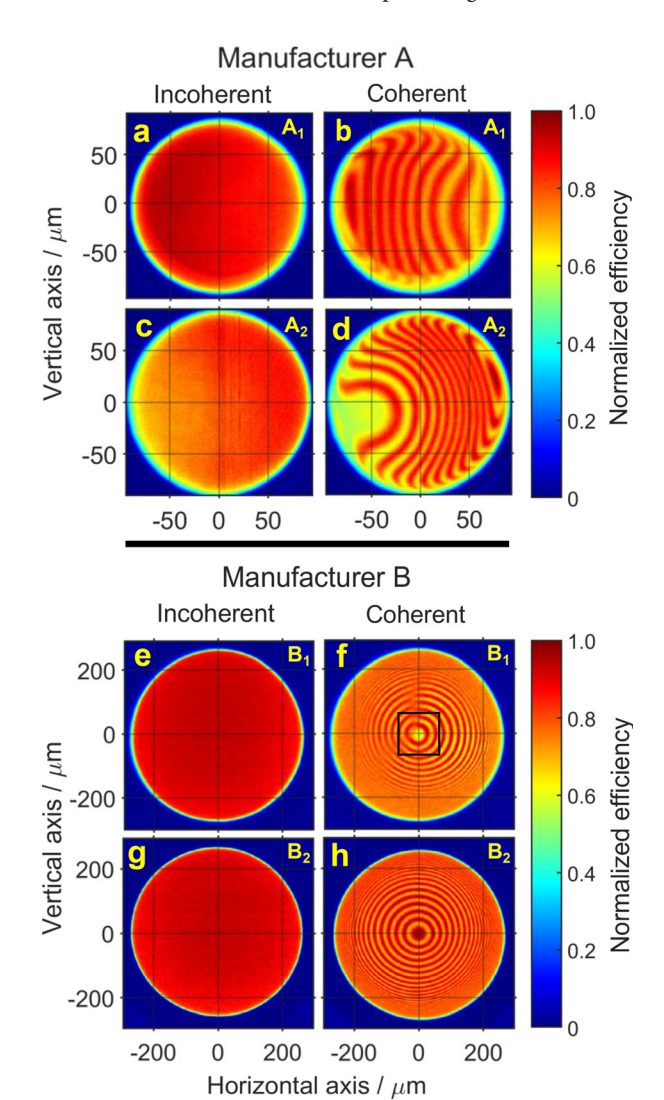


FIG. 2. Normalized spatial response maps of the four detectors. In the top right corner of each plot, a label is provided, A₁ marks detector 1 from manufacturer A, etc. The black square within sub-figure (f) marks a $120 \times 120 \,\mu\text{m}^2$ area, mapped using an alternative experimental setup—see Fig. 5. Each response was normalized with respect to their maximum efficiency value.

manufacturer **B** [Figs. 2(e)–2(h)] following the same layout. Under incoherent illumination, detectors from manufacturer **A** were found to be the least uniform: detector $\mathbf{A_1}$ has a relative slope in efficiency of -0.109% per μ m along the horizontal axis in the positive direction, whereas detector $\mathbf{B_1}$ is approximately flat in all directions. Switching to the coherent source produced spatial interference across all four detectors [i.e., Figs. 2(b), 2(d), 2(f), and 2(h)], resulting in significant variations in DE across each sensor. Similar interference patterns were observed with detectors from the same manufacturer: manufacturer \mathbf{A} 's detectors both have an axis of symmetry, with fringe spacings ranging from approximately 7 to 25 μ m, whereas detectors from manufacturer \mathbf{B} have a radial symmetry with larger spacings, ranging from approximately 10 to 30 μ m. Despite similarities between devices from the same manufacturer, clear differences are observed; for example, $\mathbf{B_1}$ has a central minimum, whereas $\mathbf{B_2}$ has a central maximum.

The intensity cross sections of detectors ${\bf A_1}$ and ${\bf B_1}$ are plotted in blue in Figs. 3(a) and 3(b), respectively. The standard definition of contrast is used, namely, $C=(I_B-I_D)/(I_B+I_D)$, where I_B and I_D are the intensities of adjacent bright and dark fringes, respectively. Contrasts up to $\approx 14\%$ were observed in the response of detector ${\bf A_1}$ and up to $\approx 18\%$ in the response of detector ${\bf B_1}$. These values correspond to respective relative efficiency variations of 25% and 30%. Contrasts of this magnitude are significantly larger than those previously reported²⁹ and are attributed to the increased spatial resolution of these measurements.

To estimate the beam waist at which the fringing is no longer visible, each cross section was convolved with Gaussian functions of varying full width at half maximum (FWHM), effectively simulating incident beams of different widths. At 20 μ m, fringing is not visible across most of detector A_1 's cross section, with the maximum contrast value being

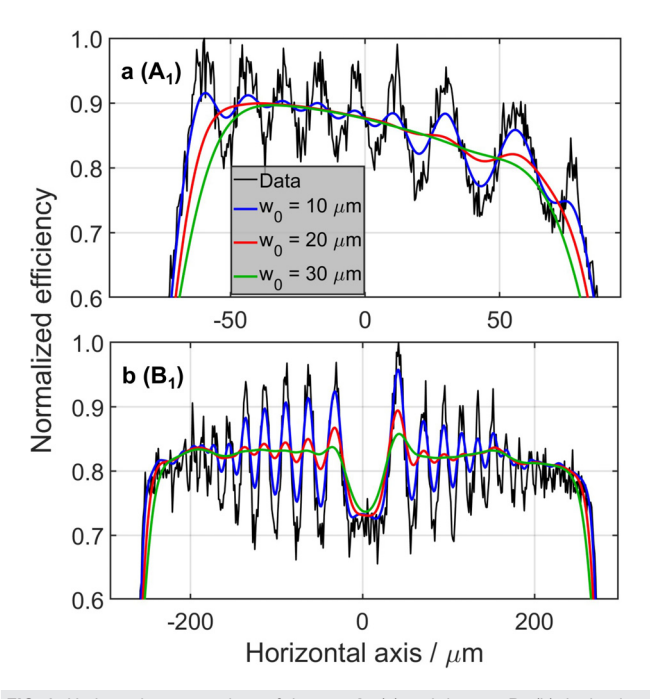


FIG. 3. Horizontal cross sections of detector $\mathbf{A_1}$ (a) and detector $\mathbf{B_1}$ (b), both taken at y=0 with reference to Fig. 2. Black marks the raw data; blue, red, and green represent the raw data convolved with Gaussian functions with FWHMs equal to 10, 20, and 30 μ m, respectively. The legend applies to both figures.

reduced to less than 2% toward one edge. At 30 μ m, the fringing is completely unresolved. In other works on devices also from manufacturer **A**, beam waists of approximately 20 μ m were used at wavelengths close to 850 nm: in one case, interference was observed, ²⁹ and in another, it was not. ¹² The 20 μ m convolution results potentially explain this inconsistency, indicating that the fringing was on the limit of being resolved. It may also be due to small variations between devices.

As a result of the greater fringe spacings and amplitudes observed in the response of detector B_1 , contrasts up to $\approx 10\%$ are still present at $20\,\mu m$. At $30\,\mu m$, the large central minima remain, with evidence of fringing still visible across the cross section. Although non-uniformities of this magnitude were not observed in the spatial response of a device also from manufacturer B when mapped using a $20\,\mu m$ beam at $810\,n m$, 37 there is evidence of interference within the response. This belief is supported by the highly uniform detector responses measured with the interference suppressed in this study.

These results emphasize that both the beam waist and coherence should be carefully considered, especially when these devices are applied to applications demanding high accuracy photon counting. Furthermore, there are other metrics that may be significantly affected as a result of the interference: for example, a SPAD's timing precision improves significantly with central excitation, ³⁸ and it also has a spot size dependence. ^{39,40} Considering detectors $\mathbf{B_1}$ and $\mathbf{B_2}$ in an application where timing response is critical, such as QKD, ⁴¹ a centrally aligned coherent beam would interfere destructively when incident upon $\mathbf{B_1}$ and constructively when incident upon $\mathbf{B_2}$, yielding a relative difference in detection efficiencies of up to 30%. Many applications require coherent light, ^{30–33} rendering these non-ideal effects unavoidable. Furthermore, this difference in DE has the potential to introduce challenges in implementing QKD security. ^{42,43}

To determine the interference source, wide-field images were taken of each detector's active area with the protective ND filters removed, and the devices switched off. The measurements were performed within the 4f optical setup outlined previously, with the inclusion of the additional components within the dashed lines of Fig. 1. Light from the 852 nm pigtailed laser diode operating above threshold was input into the setup; the beam was expanded until the sensor was overfilled by adjusting the collimation with L_1 , which effectively increased the beam's waist incident upon the sensor. The reflected light was then recorded with a CCD camera (μ Eye UI-2250-M); in all images, interference patterns consistent with their respective spatial response maps were observed. Each detector was then rotated about the optical axis (z axis, Fig. 1), and the wide-field image was observed. For A₁ and A₂, the asymmetric interference patterns clearly rotated with the SPADs. The small asymmetries present in the interference patterns of detectors B1 and B2 also rotated with the detectors. This provided confidence that the phenomenon's origin was a property of each SPAD.

The contribution of the TO-can window was assessed by removing it from a nonfunctioning detector and imaging it in the same setup. The detector, B_3 , was the same model as detectors B_1 and B_2 ; therefore, we assume it has the same physical structure. Figures 4(a) and 4(b) display the results for two different illumination spot sizes incident upon B_3 with the TO-can window removed. As this detector was not functional, the wide-field fringing could not be compared directly with its spatial response map; however, the same circular interference pattern was observed with (not shown) and without the window,

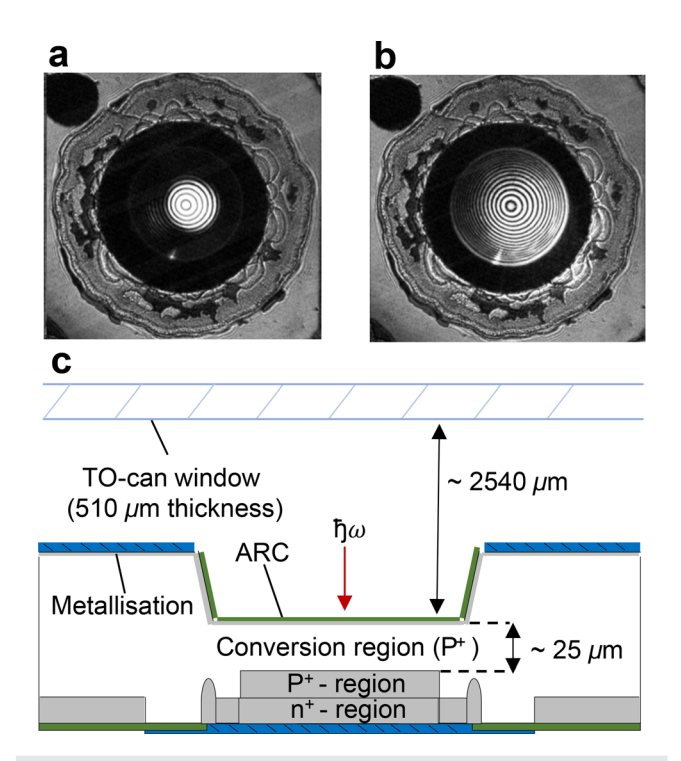


FIG. 4. (a) Gray scale image of a nonfunctioning manufacturer B detector under coherent illumination. (b) The same detector, but with the beam expanded over the active area. (c) A diagram of the APD's structure with the distances between key interfaces included. ^{37,44} In both images, the TO-can window was removed prior to measurement; it is included in the diagram for completeness.

which has comparable radial symmetry with those produced by detectors B_1 and B_2 [i.e., Figs. 2(f) and 2(h)]. This is evidence that the window is not responsible for the interference.

With reference to the device structure [Fig. 4(c)], without the window, the remaining interfaces are the air/ARC, the ARC/semiconductor, those within the internal structure of the semiconductor, and the semiconductor/rear-metalization-layer interface. Confirming that the interference effects originate within the detector's structure rather than from the window is significant because it suggests that they are intrinsic to the detectors and, therefore, are present across a broader range of SPADs. The interfaces responsible are speculated to be reflections within a passivization layer or a property of the ARCs, which are generally optimized for the peak response wavelength through quarter-wave matching: peak response is typically around 600 nm for Si-SPADs. This may explain why fringing was not observed at shorter wavelengths. In support of this, we found that by reducing the Ti: sapphire's output wavelength to ≈ 800 nm, the fringe contrasts halved in intensity.

In the case of detector $\mathbf{B_1}$, the fringes show that the DE can vary by up to $\pm 15\%$ relative to the DE measured with the interference suppressed. These variations suggest that the DE can be increased through careful alignment with a fringe maximum. To test this, we used the NPL free-space detector calibration facility, 45,46 which can accurately determine the mean photon number (μ) incident upon a detector with traceability to the primary radiometric standard—the cryogenic radiometer. The Detector $\mathbf{B_1}$ was mounted on translation stages, enabling

precise spatial response mapping of the central $120 \times 120 \, \mu \text{m}^2$ area with an $\approx 5 \, \mu \text{m}$ diameter beam in $2.5 \, \mu \text{m}$ steps. Spatial response maps measured with this set-uptake significantly longer than those produced in the 4f setup: the $120 \times 120 \, \mu \text{m}^2$ area presented in Fig. 5 took 12 h to map. This increase is primarily due to the speed at which the translation stages operate, combined with an increase in integration time at each point by a factor of 100.

The peak fringe amplitude within Fig. 5 is marked by the black circle with a diameter equal to $5\,\mu\rm m$; the beam was aligned to this point. The 852 nm pigtailed CW laser diode was used as the excitation source: it was operated below threshold (20 mA applied to the diode) to obtain the DE value with interference suppressed ($\eta_{\rm supp}$) and above threshold (150 mA applied to the diode) for the interference fringe DE value ($\eta_{\rm fringe}$). In both cases, the number of counts registered by the SPAD was set to 10^5 per second by adjusting the attenuation of the laser beam with a variable optical attenuator (Thorlabs V600A).

To calculate the DE, a time series of detector "clicks" of length T is first considered, while the detector is under a constant photon flux. T may be divided into arbitrary small time intervals δt such that there are only 1 or 0 clicks per time interval. In this scenario, the probability of the detector clicking within a time interval is calculated as $P(c|\delta t) = n_{\rm clicks} \cdot (\delta t/T)$, where $n_{\rm clicks}$ is the number of detector clicks within the time interval T. Considering the average click rate $\langle N_{\rm clicks} \rangle_{\rm T} = n_{\rm clicks} / T$, the average background count rate $\langle N_{\rm bg} \rangle_{\rm T}$, and accounting for missed events that arise from dead time losses, ⁴⁸ the probability of a click may be written as

$$P_{source}(c|\delta t) = \frac{\langle N_{\text{clicks}} - N_{\text{bg}} \rangle_{\text{T}}}{(1 - \langle N_{\text{clicks}} \rangle_{\text{T}} \cdot \tau_d)} \cdot \delta t, \tag{1}$$

where $\tau_{\rm d}$ is the detector's dead time and $T\gg\tau_{\rm d}\gg\delta t$. The "source" subscript highlights that the probability of the detector clicking is also dependent on the source statistics. To relate $P_{source}(c|\delta t)$ with an incident mean photon number μ and the detector's efficiency η , the source

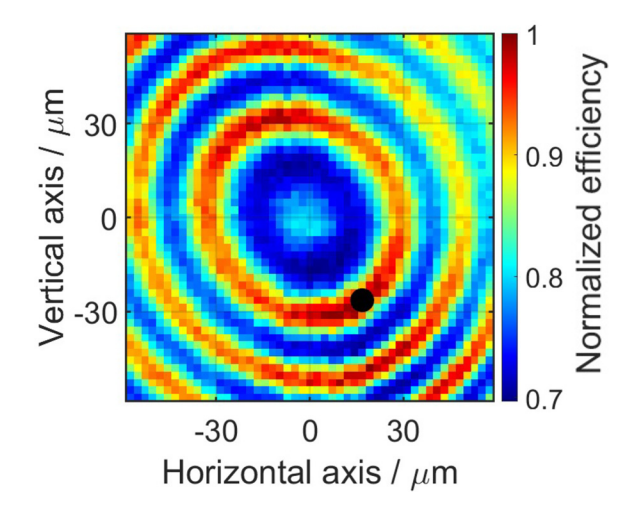


FIG. 5. The central $120 \times 120 \ \mu\text{m}^2$ responsivity map of detector **B**₁, as marked in Fig. 2(f), measured in the calibration facility while under coherent CW illumination. The values are normalized to the maximum intensity value. The black 5 μ m circle marks the location of maximum intensity—the location at which η_{supp} and η_{fringe} was measured.

statistics for the two cases were considered. Analytically, the probability of a click for the coherent source is given by

$$P_{\text{Poissonian}}(c|\delta t) = 1 - e^{-\eta \mu} \approx \eta \mu \text{ for } \eta \mu \ll 1,$$
 (2)

where μ is the mean photon number in the same time interval δ t and η is the efficiency of the detector. For the incoherent source, the statistics are assumed to be thermal, and the probability of a click is

$$P_{\text{Thermal}}(c|\delta t) = \frac{\eta \mu}{1 + \eta \mu} \approx \eta \mu \text{ for } \eta \mu \ll 1.$$
 (3)

By equating the approximated probability of a click from Eqs. (2) and (3) with Eq. (1) and solving for η , we obtain in both cases

$$\eta \approx \frac{\langle N_{\rm clicks} - N_{\rm bg} \rangle_{\rm T}}{\mu (1 - \langle N_{\rm clicks} \rangle_{\rm T} \cdot \tau_{\rm d})} \cdot \delta t. \tag{4}$$

This was verified experimentally by comparing detector clicks with a monitor photodiode's output $PD_{\rm mon}$ for both sources. Because the photodiode's output is independent of the source statistics—i.e., $PD_{\rm mon} \propto \mu$ —comparing detector click rates as a function of monitor power enables a comparison between the two. This was tested for photon flux rates up to 2×10^6 incident photons per second, and negligible differences were observed. Therefore, to ensure the SPAD was operated within its linear regime, measurements were performed below this incident photon rate, with the detector registering 10^5 cps. DE values and their absolute standard uncertainties (k=1) were

$$\eta_{supp} = 44.3(1)\%$$
 $\eta_{fringe} = 51.1(1.7)\%$.

Here, we note that η_{supp} is the value that agrees with the device's specification at the given wavelength. Therefore, by aligning the beam with a fringe maximum, a significant increase in DE is achieved; approximately 6.8% is gained in absolute value, corresponding to a 15.3% relative increase. The greater uncertainty in the η_{fringe} value stems from uncertainty in the beam's position relative to the detector's non-uniform response. This uncertainty component becomes dominant when interference is present. The uncertainty budget for η_{fringe} and calculation details are included within the supplementary material.

To conclude, we measured the spatial response maps of four commercially available SPADs from two manufacturers, illuminated by both incoherent and coherent sources. Under incoherent illumination, with interference suppressed, detectors from manufacturer B were found to be the most uniform. The uniformity of these detectors, combined with their large active areas, make them a promising tool for metrology and applications where the excitation position may vary as a function of time, providing interference is suppressed. Switching to coherent illumination produced significant interference across each detector's active area. With contrasts as high as \approx 14% and \approx 18% observed in detectors from manufacturers A and B, respectively, this phenomenon has the potential to significantly reduce the accuracy of photon counting measurements, which is especially problematic when comparing measurement scales. Through simulation, we estimated these effects can be reduced to a negligible amount by employing a beam waist greater than 20 µm with devices from manufacturer A, potentially explaining why they are not observed in some studies. However, fringing was still visible at 30 µm with devices from manufacturer B, with the central minima of B_1 still resolvable. In addition, we eliminated the TO-can window as a responsible interface by removing it, limiting the interfaces responsible to the ARCs, the surface of the semiconductor, and its internal structure. Finally, we presented a result where we leveraged the interference. By aligning a focused beam with a fringe maximum we increased the response of B_1 by $\approx [7\%$ (absolute), 15% (relative)] above specification in the near-infrared; a region of the spectrum where the responsivity of silicon SPADs declines significantly.

See the supplementary material for additional details on the detection efficiency calculations, along with an uncertainty budget.

This work was supported by the U.K. Government Department for Science, Innovation and Technology through the U. K. National Quantum Technologies Programme. We also highlight the work of the Istituto Nazionale di Ricerca Metrologica (INRiM) on interference effects in SPADs, which was originally presented by Giorgio Brida at the NEWRAD 2023 conference. ³⁴ We thank Simon R. G. Hall for his valuable contributions through constructive discussions. P.R. Dolan's current affiliation is with NU QUANTUM LTD, 21 JJ Thomson Avenue, Cambridge CB3 0FA, U.K.

AUTHOR DECLARATIONS Conflict of Interest

The authors have no conflicts to disclose.

Author Contributions

L. Arabskyj: Conceptualization (equal); Formal analysis (lead); Investigation (lead); Methodology (equal); Validation (equal); Visualization (equal); Writing – original draft (lead); Writing – review & editing (supporting). B. Dejen: Investigation (supporting); Methodology (equal); Writing – review & editing (supporting). T. S. Santana: Formal analysis (supporting); Methodology (supporting); Writing – review & editing (supporting); Writing – review & editing (supporting); Visualization (equal); Writing – review & editing (equal). C. J. Chunnilall: Conceptualization (supporting); Funding acquisition (equal); Supervision (supporting); Validation (equal); Visualization (equal); Writing – review & editing (lead). P. R. Dolan: Conceptualization (equal); Formal analysis (supporting); Funding acquisition (equal); Methodology (equal); Supervision (lead); Validation (equal); Visualization (equal); Writing – original draft (supporting); Writing – review & editing (supporting); Writing – review & editing (supporting);

DATA AVAILABILITY

The data that support the findings of this study are available from the corresponding author upon reasonable request.

REFERENCES

¹C. J. Chunnilall, I. P. Degiovanni, S. Kück, I. Müller, and A. G. Sinclair, "Metrology of single-photon sources and detectors: A review," Opt. Eng. 53, 081910 (2014).

²F. Villa, F. Severini, F. Madonini, and F. Zappa, "SPADs and SiPMs arrays for long-range high-speed light detection and ranging (LiDAR)," Sensors 21, 3839 (2021).

³J. Rapp, J. Tachella, Y. Altmann, S. McLaughlin, and V. K. Goyal, "Advances in single-photon lidar for autonomous vehicles: Working principles, challenges, and recent advances," IEEE Signal Process. Mag. 37, 62–71 (2020).

- ⁴F. Zappa and A. Tosi, "MiSPIA: Microelectronic single-photon 3D imaging arrays for low-light high-speed safety and security applications," Proc. SPIE 8727, 87270L (2013).
- ⁵H.-H. Huang, T.-Y. Huang, C.-H. Liu, S.-D. Lin, and C.-Y. Lee, " 32×64 SPAD imager using 2-bit in-pixel stack-based memory for low-light imaging," IEEE Sens. J. 23, 19272–19281 (2023).
- ⁶C. Bruschini, H. Homulle, I. M. Antolovic, S. Burri, and E. Charbon, "Single-photon avalanche diode imagers in biophotonics: Review and outlook," Light **8**, 87 (2019).
- ⁷M. L. Rastello, I. P. Degiovanni, A. G. Sinclair, S. Kück, C. J. Chunnilall, G. Porrovecchio, M. Smid, F. Manoocheri, E. Ikonen, T. Kubarsepp *et al.*, "Metrology for industrial quantum communications: The MIQC project," Metrologia 51, S267 (2014).
- ⁸L. Arabskyj, P. R. Dolan, A. L. Parke, T. S. Santana, S. R. Hall, G. Porrovecchio, M. Smid, M. Lucamarini, and C. J. Chunnilall, "Traceable characterisation of fibre-coupled single-photon detectors," Metrologia 61, 055008 (2024).
- ⁹I.-H. Bae, S. Park, K.-S. Hong, H. S. Park, H. J. Lee, H. S. Moon, J. S. Borbely, and D.-H. Lee, "Detection efficiency measurement of single photon avalanche photodiodes by using a focused monochromatic beam tunable from 250 nm to 1000 nm," Metrologia 56, 035003 (2019).
- ¹⁰M. López, H. Hofer, and S. Kück, "Detection efficiency calibration of single-photon silicon avalanche photodiodes traceable using double attenuator technique," J. Mod. Opt. 62, 1732–1738 (2015).
- ¹¹G. Brida, S. Castelletto, I. Degiovanni, C. Novero, and M. L. Rastello, "Quantum efficiency and dead time of single-photon counting photodiodes: A comparison between two measurement techniques," Metrologia 37, 625 (2000).
- ¹²J. Jin, T. Gerrits, and A. Gamouras, "Calibration and comparison of detection efficiency for free-space single-photon avalanche diodes at 850 nm," Appl. Opt. 61, 5244–5249 (2022).
- ¹³M. López, A. Meda, G. Porrovecchio, R. Starkwood, M. Genovese, G. Brida, M. Šmid, C. Chunnilall, I. Degiovanni, and S. Kück, "A study to develop a robust method for measuring the detection efficiency of freerunning InGaAs/InP single-photon detectors," EPJ Quantum Technol. 7, 14 (2020).
- ¹⁴G. Porrovecchio, M. Šmid, M. López, H. Hofer, B. Rodiek, and S. Kück, "Comparison at the sub-100 fW optical power level of calibrating a singlephoton detector using a high-sensitive, low-noise silicon photodiode and the double attenuator technique," <u>Metrologia</u> 53, 1115 (2016).
- ¹⁵J. Y. Cheung, C. J. Chunnilall, G. Porrovecchio, M. Smid, and E. Theocharous, "Low optical power reference detector implemented in the validation of two independent techniques for calibrating photon-counting detectors," Opt. Express 19, 20347–20363 (2011).
- ¹⁶S. V. Polyakov and A. L. Migdall, "High accuracy verification of a correlated-photon-based method for determining photon-counting detection efficiency," Opt. Express 15, 1390–1407 (2007).
- ¹⁷J. C. Bienfang, T. Gerrits, P. S. Kuo, A. Migdall, S. Polyakov, and O. Slattery, "Single-photon sources and detectors dictionary," Report No. 8486 (National Institute of Standards and Technology, Gaithersburg, MD, 2023).
- ¹⁸Z. Yuan, A. Plews, R. Takahashi, K. Doi, W. Tam, A. Sharpe, A. Dixon, E. Lavelle, J. Dynes, A. Murakami *et al.*, "10-Mb/s quantum key distribution," J. Lightwave Technol. **36**, 3427–3433 (2018).
- ¹⁹A. Dixon, J. Dynes, M. Lucamarini, B. Fröhlich, A. Sharpe, A. Plews, S. Tam, Z. Yuan, Y. Tanizawa, H. Sato *et al.*, "High speed prototype quantum key distribution system and long term field trial," Opt. Express 23, 7583–7592 (2015).
- ²⁰L. C. Comandar, B. Fröhlich, M. Lucamarini, K. A. Patel, A. W. Sharpe, J. F. Dynes, Z. L. Yuan, R. V. Penty, and A. J. Shields, "Room temperature single-photon detectors for high bit rate quantum key distribution," Appl. Phys. Lett. 104, 021101 (2014).
- ²¹M. Lucamarini, K. Patel, J. Dynes, B. Fröhlich, A. Sharpe, A. Dixon, Z. Yuan, R. Penty, and A. Shields, "Efficient decoy-state quantum key distribution with quantified security," Opt. Express 21, 24550–24565 (2013).
- ²²Q. Zhang, H. Takesue, T. Honjo, K. Wen, T. Hirohata, M. Suyama, Y. Takiguchi, H. Kamada, Y. Tokura, O. Tadanaga *et al.*, "Megabits secure key rate quantum key distribution," New J. Phys. 11, 045010 (2009).

- ²³S. Ecker, B. Liu, J. Handsteiner, M. Fink, D. Rauch, F. Steinlechner, T. Scheidl, A. Zeilinger, and R. Ursin, "Strategies for achieving high key rates in satellite-based QKD," npj Quantum Inf. 7, 5 (2021).
- ²⁴J. Dynes, A. Wonfor, W.-S. Tam, A. Sharpe, R. Takahashi, M. Lucamarini, A. Plews, Z. Yuan, A. Dixon, J. Cho et al., "Cambridge quantum network," npj Quantum Inf. 5, 101 (2019).
- ²⁵A. Dixon, J. Dynes, M. Lucamarini, B. Fröhlich, A. Sharpe, A. Plews, W. Tam, Z. Yuan, Y. Tanizawa, H. Sato *et al.*, "Quantum key distribution with hacking countermeasures and long term field trial," Sci. Rep. 7, 1978 (2017).
- ²⁶R. Ursin, F. Tiefenbacher, T. Schmitt-Manderbach, H. Weier, T. Scheidl, M. Lindenthal, B. Blauensteiner, T. Jennewein, J. Perdigues, P. Trojek et al., "Entanglement-based quantum communication over 144 km," Nat. Phys. 3, 481–486 (2007).
- ²⁷M. Avesani, L. Calderaro, M. Schiavon, A. Stanco, C. Agnesi, A. Santamato, M. Zahidy, A. Scriminich, G. Foletto, G. Contestabile *et al.*, "Full daylight quantum-key-distribution at 1550 nm enabled by integrated silicon photonics," npj Quantum Inf. 7, 93 (2021).
- ²⁸A. Migdall, S. Castelletto, I. P. Degiovanni, and M. L. Rastello, "Intercomparison of a correlated-photon-based method to measure detector quantum efficiency," Appl. Opt. 41, 2914–2922 (2002).
- 29T. Gerrits, A. Migdall, J. C. Bienfang, J. Lehman, S. W. Nam, J. Splett, I. Vayshenker, and J. Wang, "Calibration of free-space and fiber-coupled single-photon detectors," Metrologia 57, 015002 (2020).
- ³⁰P. Keshavarzian, K. Ramu, D. Tang, C. Weill, F. Gramuglia, S. S. Tan, M. Tng, L. Lim, E. Quek, D. Mandich, M. Stipčević, and E. Charbon, "A 3.3-Gb/s SPAD-based quantum random number generator," IEEE J. Solid-State Circuits 58, 2632–2647 (2023).
- ³¹M. Avesani, H. Tebyanian, P. Villoresi, and G. Vallone, "Unbounded randomness from uncharacterized sources," Commun. Phys. 5, 273 (2022).
- ³²M. Pittaluga, M. Minder, M. Lucamarini, M. Sanzaro, R. I. Woodward, M.-J. Li, Z. Yuan, and A. J. Shields, "600-km repeater-like quantum communications with dual-band stabilization," Nat. Photonics 15, 530–535 (2021).
- ³³M. Lucamarini, Z. L. Yuan, J. F. Dynes, and A. J. Shields, "Overcoming the rate-distance limit of quantum key distribution without quantum repeaters," Nature 557, 400–403 (2018).
- 34S. Virzi, A. Meda, E. Redolfi, M. Gramegna, G. Brida, M. Genovese, and I. P. Degiovanni, "Detection efficiency characterization for free-space single-photon detectors: Measurement facility and wavelength-dependence investigation," arXiv:2407.01120 (2024).
- 35K. Dhoska, H. Hofer, B. Rodiek, M. López, T. Kübarsepp, and S. Kück, "Improvement of the detection efficiency calibration and homogeneity measurement of Si-SPAD detectors," SpringerPlus 5(1–14), 2065 (2016).
- 36M. Hofbauer, K. Schneider-Hornstein, and H. Zimmermann, Single-Photon Detection for Data Communication and Quantum Systems (IOP Publishing, 2021), pp. 2053–2563.
- 37 M. Stipčević, D. Wang, and R. Ursin, "Characterization of a commercially available large area, high detection efficiency single-photon avalanche diode," J. Lightwave Technol. 31, 3591–3596 (2013).
- ³⁸M. Assanelli, A. Ingargiola, I. Rech, A. Gulinatti, and M. Ghioni, "Photon-timing jitter dependence on injection position in single-photon avalanche diodes," IEEE J. Quantum Electron. 47, 151–159 (2011).
- ³⁹A. Spinelli, L. Davis, and H. Dautet, "Actively quenched single-photon avalanche diode for high repetition rate time-gated photon counting," Rev. Sci. Instrum. 67, 55–61 (1996).
- ⁴⁰L.-Q. Li and L. M. Davis, "Single photon avalanche diode for single molecule detection," Rev. Sci. Instrum. 64, 1524–1529 (1993).
- ⁴¹A. Lee, A. T. Castillo, C. Whitehill, and R. Donaldson, "The impact of spot-size on single-photon avalanche diode timing-jitter and quantum key distribution," IET Quantum Commun. (published online 2024).
- ⁴²C.-H. F. Fung, K. Tamaki, B. Qi, H.-K. Lo, and X. Ma, "Security proof of quantum key distribution with detection efficiency mismatch," QIC. 9, 131–0165 (2009).
- ⁴³V. Makarov, A. Anisimov, and J. Skaar, "Effects of detector efficiency mismatch on security of quantum cryptosystems," Phys. Rev. A 74, 022313 (2006).
- 44M. Stipčević, B. G. Christensen, P. G. Kwiat, and D. J. Gauthier, "Advanced active quenching circuit for ultra-fast quantum cryptography," Opt. Express 25, 21861–21876 (2017).

⁴⁵C. J. Chunnilall, L. Arabskyj, R. A. Starkwood *et al.*, "Calibration of free-space single-photon detectors," (unpublished).

⁴⁶ National Physical Laboratory, see https://www.npl.co.uk/quantum-programme/ capabilities/photon-detector for "Single-photon detector calibration" (2024); accessed: October 1, 2024.

 ⁴⁷J. Martin, N. Fox, and P. Key, "A cryogenic radiometer for absolute radiometric measurements," Metrologia 21, 147 (1985).
 ⁴⁸E. Sciacca, A. C. Giudice, D. Sanfilippo, F. Zappa, S. Lombardo, R. Consentino, C. Di Franco, M. Ghioni, G. Fallica, G. Bonanno *et al.*, "Silicon planar technology for single-photon optical detectors," IEEE Trans. Electron Devices 50, 918–925 (2003).